Modifying the geometric and electronic structure of hexagonal boron nitride on Ir(111) by Cs adsorption and intercalation

Jiaqi Cai,[1,2,3] Wouter Jolie,[2] Caio C. Silva,[1,2] Marin Petrović,[4] Christoph Schlueter,[5] Thomas Michely,[2] Marko Kralj,[4] Tien-Lin Lee,[5] and Carsten Busse[1,2,3,*]

[1]*Institut für Materialphysik, Westfälische Wilhelms-Universität Münster, Wilhelm-Klemm-Straße 10, 48149 Münster, Germany*

[2]*II. Physikalisches Institut, Universität zu Köln, Zülpicher Straße 77, 50937 Köln, Germany*

[3]*Department Physik, Universität Siegen, Walter-Flex-Straße 3, 57068 Siegen, Germany*

[4]*Center of Excellence for Advanced Materials and Sensing Devices, Institute of Physics, Bijenička 46, 10000 Zagreb, Croatia*

[5]*Diamond Light Source, Didcot OX11 0DE, Oxfordshire, United Kingdom*

(Received 14 June 2018; revised manuscript received 18 October 2018; published 28 November 2018)

Epitaxial hexagonal boron nitride on Ir(111) is significantly modified by adsorption and intercalation of alkali-metal atoms. Regarding geometry, intercalation lifts the two-dimensional layer from its substrate and reduces the characteristic corrugation imprinted by direct contact with the metal substrate. Moreover, the presence of charged species in close proximity to the hexagonal boron nitride (hBN) layer strongly shifts the electronic structure (valence bands and core levels). We used scanning tunneling microscopy, low-energy electron diffraction, x-ray photoelectron spectroscopy (XPS), and the x-ray standing wave technique to study changes in the atomic structure induced by Cs adsorption and intercalation. Depending on the preparation, the alkali-metal atoms can be found on top and underneath the hexagonal boron nitride in ordered and disordered arrangements. Adsorbed Cs does not change the morphology of hBN/Ir(111) significantly, whereas an intercalated layer of Cs decouples the two-dimensional sheet and irons out its corrugation. XPS and angle-resolved photoelectron spectroscopy reveal a shift of the electronic states to higher binding energies, which increases with increasing density of the adsorbed and intercalated Cs. In the densest phase, Cs both intercalates and adsorbs on hBN and shifts the electronic states of hexagonal boron nitride by 3.56 eV. As this shift is not sufficient to move the conduction band below the Fermi energy, the electronic band gap must be larger than 5.85 eV.

DOI: 10.1103/PhysRevB.98.195443

I. INTRODUCTION

Monolayer hexagonal boron nitride (hBN) is graphene's isostructural, yet insulating, counterpart. Due to its wide band gap, flatness, and chemical inertness it is an ideal substrate for graphene [1], monolayers of transition-metal dichalcogenides [2], and organic molecules [3]. Furthermore, it plays an essential role as the insulating layer in functionalized van der Waals heterostructures operating as field-effect transistors [4] or light-emitting diodes [5].

Even though the wide band gap is one of the most appealing features of hBN, important characteristics of its band structure remain unclear. In density functional theory (DFT) calculations, both direct [6–8] and indirect [6,9–12] band gaps have been reported, and the band gap size varies from 4.3 eV [10] to 6.86 eV [6]. Experimental efforts also yield no consistent results. Scanning tunneling spectroscopy measures a 5 eV band gap on hBN/Ir(111) [13], whereas optical absorption spectroscopy reveals a 6.07 eV optical band gap [14–16]. Monolayer hBN shares this problem with its bulk parent compound (which has a significantly different band structure due to the absence of confinement effects and the larger unit cell), where neither the nature of the band gap (direct or indirect) nor its magnitude is established: for bulk hBN, DFT consistently yields an indirect band gap with the bottom of the conduction band at the M point and the top of the valence band at the K point of the surface Brillouin zone [10,17], but the band gap size varies among different calculations and methods from 3.9 to 5.95 eV. Experimentally, Watanabe *et al.* measured a direct band gap of 5.971 eV [18] based on the much higher photoluminescence intensity in comparison to diamond (indirect band gap). Cassabois *et al.* recently conducted a similar measurement at low temperature and found a more finely structured photoluminescence spectrum, leading to an indirect band gap of 5.955 eV [19].

In our study, we exploit a common feature of two-dimensional (2D) materials, namely, that their properties can be strongly modified by other substances in close contact. These substances can be the substrate [20] or adsorbed as well as intercalated atoms and molecules [21,22]. Due to their low ionization energy, modifications of the electronic structure can be effectively induced by alkali-metal atoms, which can be either adsorbed on the 2D material or intercalated between the ultrathin sheet and its substrate. This has been demonstrated both for epitaxial graphene [21,23–26] and for epitaxial hBN [27].

The mechanism governing the changes in electronic structure differs between the zero-band-gap semiconductor graphene and the large-band-gap insulator hBN: for graphene, the charge from the alkali atoms transfers (at least partially) to the graphene $\pi^\star$ band. Due to this doping, previously

*carsten.busse@uni-siegen.de

unoccupied bands shift below the Fermi energy and become detectable by angle-resolved photoelectron spectroscopy (ARPES) [21,23–26]. This is not the case for hBN because of the large band gap. Here, a good starting point to describe the shift of the band structure is the vacuum level alignment approach that predicts the top of the valence band at a binding energy of $E_v = E_i - \Phi$, where E_i is the ionization energy of hBN and Φ is the work function of the substrate (we adhere to the standard in photoelectron spectroscopy and denote binding energies as positive values). In the conceptually simplest case of alkali-metal intercalation, it is sufficient to consider only the reduction of Φ due to the surface dipole from the positively charged alkali ions adsorbed on top of the metal substrate: when Φ changes by $\Delta\Phi = \Phi' - \Phi$, E_v changes by $\Delta E = E_v' - E_v = -\Delta\Phi$. A large increase (that can be induced by a large reduction in work function) is worth pursuing in order to pull the hBN conduction band below the Fermi energy and finally enable its population with donated electrons (see also [28]). Therefore, the band gap of hBN could be determined using ARPES. When the alkali-metal atoms are not intercalated but adsorbed (or even both), the situation gets more complicated but is still similar to the above picture: one has to replace the difference in work function $\Delta\Phi$ by the local electric potential energy $e\phi(h_{hBN})$ at the position of the hBN sheet. Here, we assume that the electric potential $\phi(h)$ is constant parallel to the surface and define $\phi(-\infty) = 0$ deep in the bulk, and thus, $\Delta E = e\phi(h)$. The change in sign is due to the fact that the work function is defined as the work needed to bring an electron from the bulk to the vacuum, whereas the potential is defined by the work done on a positive charge. Under the assumption of a rigid shift the whole band structure $E(\vec{k})$ moves by ΔE in binding energy. A related change can also be expected for the core levels.

Intercalation also significantly changes the geometric structure of 2D materials epitaxially grown on metal substrates. To give an example, intercalation of H and CO reduces the moiré corrugation of hBN/Rh(111) [29,30]. This decoupling of hBN from its substrate also leads to the relaxation of the stress in the hBN layer, which is observed as an expansion of the Brillouin zone [31].

In this paper, we report our experimental investigation of the modification of hBN/Ir(111) by exposure to Cs at different temperatures, leading to adsorption and intercalation. We choose Cs due to its very low ionization energy, where a larger shift of the hBN bands can be expected compared with previous studies using Li and K [27]. The scanning tunneling microscopy (STM) and low-energy electron diffraction (LEED) results are discussed first, and the relative vertical positions of Cs in different morphologies are proposed. This is then followed by results from x-ray photoelectron spectroscopy (XPS), x-ray standing wave (XSW), and ARPES, which confirm the different positions of Cs suggested by STM and LEED. The influence of the incorporated Cs on the geometric structure, as well as the electronic structure of hBN, is discussed in detail.

II. EXPERIMENTAL DETAILS

The experiments were performed in three ultrahigh vacuum (UHV) setups. STM measurements were performed in Cologne, at low temperature ($T = 5$ K) and a base pressure lower than 5×10^{-11} mbar. The STM images were postprocessed using WSXM [32]. ARPES measurements were performed in Zagreb at room temperature (RT). The base pressure of the ARPES chamber was lower than 1×10^{-9} mbar. A helium discharge ultraviolet lamp (photon energy of 21.2 eV, beam spot diameter of ~2 mm) was used for the excitation. The XPS and XSW experiments were carried out at Beamline I09 of the Diamond Light Source at RT, where the base pressure was lower than 2×10^{-10} mbar.

The Ir(111) surface was cleaned in ultrahigh vacuum by irradiation by 1.5 keV Ar^+ ions at RT followed by annealing to 1473 K. The cleanliness of the surface was checked by LEED. A full layer of hBN was prepared using chemical vapor deposition (CVD): the Ir substrate was kept at 1273–1373 K in a borazine ($B_3H_6N_3$) atmosphere (2×10^{-7} mbar). A pronounced moiré pattern appearing in LEED [Fig. 1(d)] is evidence of the high quality of the hBN. Cs was deposited from a commercial source (SAES Getters) onto hBN/Ir(111). The evaporation time was always sufficient to ensure saturation. In our home labs a fresh layer of hBN was grown for every Cs deposition, while at the synchrotron, CVD was performed only once to reduce the exposure of the system to borazine. The sequential series of adsorption, intercalation,

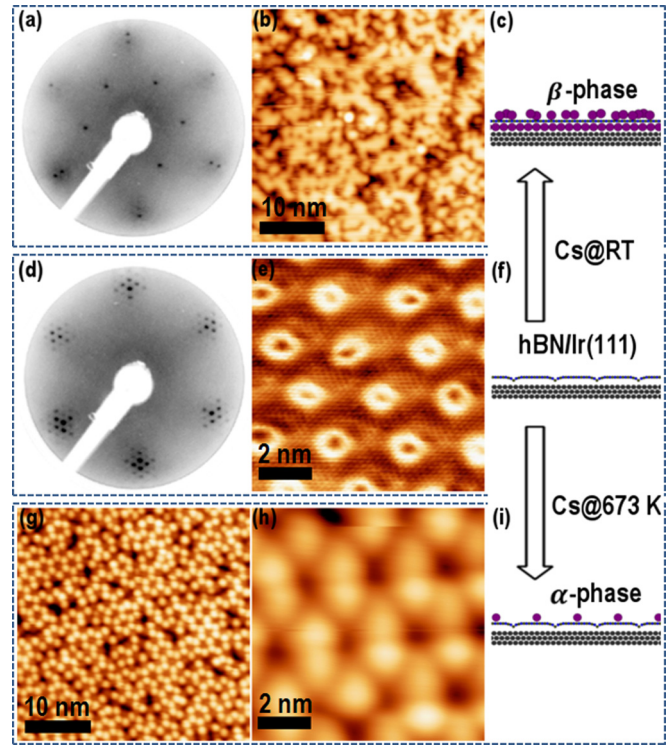

FIG. 1. (a)–(c) The β phase: (a) inverse contrast 157.5 eV LEED pattern, (b) 50×50 nm^2 STM image (bias voltage of -2.0 V, tunneling current of 3.1×10^{-11}A), and (c) structural model. (d)–(f) hBN/Ir(111): (d) inverse contrast 157.5 eV LEED pattern, (e) 10×10 nm^2 STM image (bias voltage of 0.068 V, tunneling current of 1.7×10^{-10} A), and (f) structural model. (g)–(i) The α phase: (g) 50×50 nm^2 STM image (bias voltage of 3.0 V, tunneling current of 1.0×10^{-10} A), (h) 10×10 nm^2 STM image (bias voltage of 2.0 V, tunneling current of 5.1×10^{-11} A), and (i) structural model.

and deintercalation can lead to small holes in the hBN layer, exposing the bare Ir substrate.

For XSW measurements, we used a defocused beam to minimize beam damage. Photoelectrons were collected from an emission angle of $\theta = 60^\circ$ up to $\theta = 90^\circ$. We measured XSW curves on three different spots on the sample for N 1*s* and B 1*s* and two different spots for Cs $3d_{5/2}$. The results were nearly identical, indicating a very homogeneous sample. In addition, we recorded x-ray photoelectron spectra before and after each XSW scan. The spectra showed nearly no differences, indicating negligible beam damage. For XPS and XSW analysis, the spectra were approximated by a sum of Gaussian components, after subtraction of a linear background. The XSW analysis was performed using a self-written script based on dynamical diffraction theory of x rays. Our reference value for the interlayer distance of Ir(111) is 2.2167 Å [33]. We include nondipole corrections, and the values of the forward-backward asymmetry parameters are $Q_B = 0.10$, $Q_N = 0.09$, and $Q_{Cs} = 0.07$. These parameters are calculated assuming an angle of 19° between the photon polarization vector and the photoemission direction and using the tabulated dipolar asymmetry parameters and the asymmetry factors associated with the interference between the electric dipole and electric quadrupole [34].

For more experimental details about hBN growth, STM, XPS, and XSW measurements see Ref. [20]. For more experimental details about the ARPES measurement see Ref. [35].

III. RESULTS AND DISCUSSION

Cs deposition until saturation onto pristine hBN/Ir(111) at RT leads to a Cs-rich phase (β phase). LEED shows a clear $(\sqrt{3} \times \sqrt{3})$R30° superstructure relative to the first-order diffraction spots of Ir(111), and the moiré pattern is no longer visible [Fig. 1(a)]. This commensurate LEED pattern suggests the presence of an ordered layer of Cs in direct contact with the Ir substrate surface, which intercalates hBN and decouples it from the substrate surface, thus lifting the moiré pattern. At the same time, additional Cs adsorbs on top, appearing granular and unstructured on the nanometer scale in STM measurements [Fig. 1(b)]. Figure 1(c) shows a structural model that is consistent with our LEED and STM observations.

When Cs is deposited while keeping the hBN/Ir(111) substrate at 673 K, another phase (α phase) forms. STM imaging [Fig. 1(g)] reveals a honeycomb lattice of bright protrusions [see also the large-scale image in Fig. 1(h)]. These protrusions can be removed using extreme tunneling conditions (high negative bias voltage, close tip approach), leaving behind pristine hBN/Ir(111). Based on this finding, we identify the bright protrusions in the α phase as adsorbed Cs atoms on top of hBN. The lateral ordering of the adatoms into a honeycomb structure (induced by the hBN moiré) is intriguing but not relevant for the changes to the electronic structure focused on here. It will be discussed elsewhere. Figure 1(i) illustrates the structural model we propose for the α phase. Finding such a dilute phase in spite of evaporating approximately the same amount of Cs as for the much denser β phase indicates that Cs is able to desorb efficiently from hBN at 673 K from all but the most stable adsorption sites. This leads to an upper limit of the Cs coverage achievable at 673 K, which seems to be lower than the threshold needed for Cs intercalation [24].

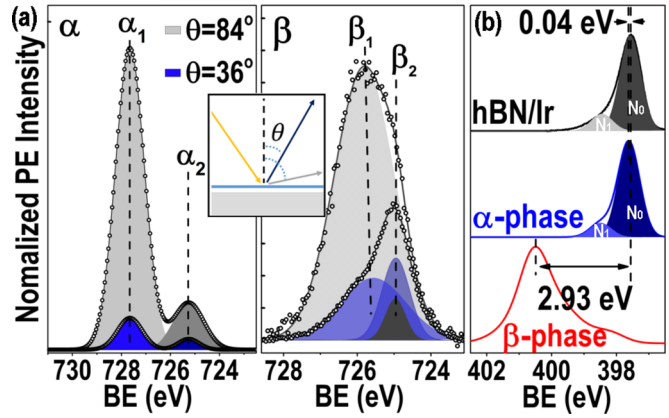

FIG. 2. (a) Normalized Cs $3d_{5/2}$ PE spectra measured on the α and β phases at large ($\theta = 84^\circ$, gray) and small ($\theta = 36^\circ$, blue) emission angles, with 900 eV soft x rays. The inset is the sketch of the two measurement configurations at large (gray) and small (blue) emission angles. (b) Comparison of PE N 1*s* spectra measured on pristine hBN/Ir(111) (black), the α phase (blue), and the β phase (red). Two components are fitted to the spectra, representing the strongly and weakly bonded areas of hBN. N 1*s* XPS spectra are measured with 575 eV soft x rays.

In principle, one can expect more phases in our system, for example, only orderly intercalated Cs without further adsorption on top of hBN. Experimentally, we did not achieve this intercalation-only phase, indicating that phase space in temperature and coverage for other structures is very small or even zero.

The two phases with very different Cs densities (low in the α phase and high in the β phase) are studied in detail using photoemission (PE) methods (XPS, ARPES, XSW). Starting with the α phase, the Cs $3d_{5/2}$ PE spectra are presented in the left panel of Fig. 2(a). Two components are resolved: a dominating high-binding-energy component α_1 at 727.66 eV and a minority low-binding-energy component α_2 at 725.28 eV. The Cs $3d_{3/2}$ spectra exhibit the same double-peak feature (not shown).

We recorded spectra at near normal ($\theta = 36^\circ$) and grazing ($\theta = 84^\circ$) emission angles and normalized the Cs $3d_{5/2}$ intensity I_{Cs} to the N 1*s* intensity I_N [see the inset of Fig. 2(a)]. Therefore, we can get a first indication of the position of the Cs: when the alkali metal is located underneath hBN, the photoelectrons emitted from it are partially scattered by the 2D material, and this attenuation increases with increasing θ, leading to a reduction in I_{Cs}/I_N [21]. Conversely, when I_{Cs}/I_N does not decrease with increasing θ, we can conclude that Cs is not buried beneath hBN. Note, however, that in this case we cannot distinguish between Cs adsorbed on top of hBN and Cs adsorbed on pristine Ir(111).

We find that for the α phase, the normalized intensity of the dominating α_1 component increases with emission angle from $I^{\alpha_1}_{Cs}/I_N(36^\circ) = 0.16$ to $I^{\alpha_1}_{Cs}/I_N(84^\circ) = 1.39$, indicating that the emitters are not intercalated underneath hBN. Based on the high intensity, the chemical shifts (see below), and the

TABLE I. Comparison of pristine hBN/Ir(111) and the α-phase N 1*s* PE spectra: positions of N_0 and N_1 as well as their FWHM.

	hBN/Ir(111) [20]	α Phase
N_0	397.58	397.62
N_1	398.46	398.49
FWHM	0.79	0.79

position relative to hBN, we assign the α_1 component to Cs atoms on top of hBN.

We assign the minority α_2 component to Cs atoms adsorbed directly on uncovered patches of Ir(111) based on four findings: (i) the overall intensity of this component is low, (ii) $I_{\mathrm{Cs}}^{\alpha_2}/I_{\mathrm{N}}(36^\circ) = 0.06$ increases to $I_{\mathrm{Cs}}^{\alpha_2}/I_{\mathrm{N}}(84^\circ) = 0.24$, (iii) the core level shift is similar to the one found for intercalated Cs, i.e., Cs in direct contact with Ir(111) (see below), and (iv) the coherent position determined by XSW is similar to the one of intercalated Cs. A possible origin of the bare Ir surface is the repeated intercalation/deintercalation as described in Sec. II.

The blue curve in Fig. 2(b) shows the N 1*s* PE spectrum from an α-phase sample. A dominating component (N_0) is found at 397.62 eV, and a small shoulder (N_1) appears at 398.49 eV. Only minor changes are found when comparing this double-peak structure to pristine hBN/Ir(111) (black curve, top panel; see also [20]), which are summarized in Table I: the energy separation between N_0 and N_1 (~0.87 eV) and the peak full width at half maximum (FWHM ~0.79 eV) are identical. This resemblance (also found for B 1*s*, not shown) indicates that Cs adsorbed at low concentration induces no major changes in hBN/Ir(111), which is more evidence of the nonintercalated nature of Cs in the α phase. The N_0 and N_1 components can therefore be assigned to the weakly and strongly bound areas in the moiré unit cell, respectively, identical to pristine hBN/Ir(111). The small shifts (~0.04 eV) observed in the positions of the core levels may still be significant as they follow the much larger shifts of the valence bands (see below).

Preliminary XSW measurements also support our model for the α_1-Cs (adsorbed on hBN): the relative height above the virtual sample surface calculated from the coherent position is 6.54 Å, while the relative height of the hill regions of hBN is 3.63 Å. A full study of the details of the geometry of this phase is under way.

The right panel of Fig. 2(a) shows the Cs $3d_{5/2}$ PE spectra of the β phase. The Cs $3d_{5/2}$ peak contains two components, one at 725.57 eV (β_1) and another at a lower binding energy of 724.95 eV (β_2). The spectra are again measured at different emission angles and normalized to the corresponding N 1*s* intensity to investigate the relative vertical location of Cs. $I_{\mathrm{Cs}}/I_{\mathrm{N}}(\theta)$ of the two components behave very differently: the β_1 component is stronger at a large emission angle [$I_{\mathrm{Cs}}^{\beta_1}/I_{\mathrm{N}}(36^\circ) = 0.10$, $I_{\mathrm{Cs}}^{\beta_1}/I_{\mathrm{N}}(84^\circ) = 0.81$], whereas the β_2 component is stronger at a small emission angle [$I_{\mathrm{Cs}}^{\beta_2}/I_{\mathrm{N}}(36^\circ) = 0.20$, $I_{\mathrm{Cs}}^{\beta_2}/I_{\mathrm{N}}(84^\circ) = 0.07$]. Based on this observation, we assign the β_1 component to Cs adsorbed on hBN and the β_2 component to ordered intercalated Cs. We notice a small difference of the β_1-component binding energy measured at different emission angles (725.57 eV at $\theta = 36^\circ$ and 725.81 eV at $\theta = 84^\circ$). We assign this uncertainty to the disordered nature of the adsorbed Cs on top of hBN. Details about the stacking structure of the adsorbed Cs are hidden in this angle dependence.

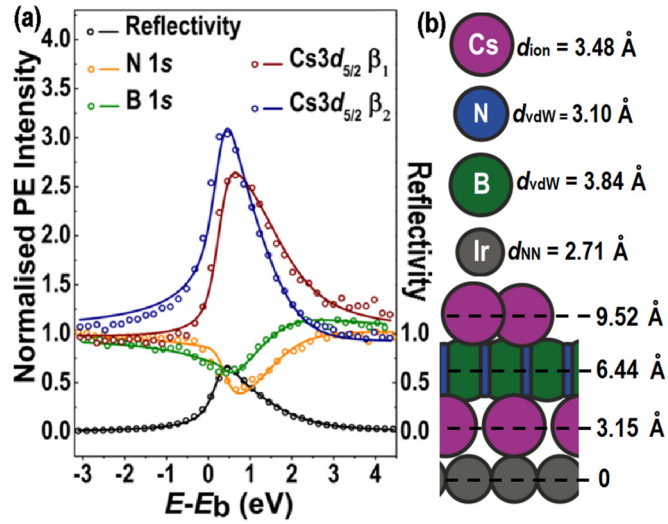

FIG. 3. (a) XSW results for N 1*s* and B 1*s* and HBE and LBE components of Cs $3d_{5/2}$, with measured data given as circles and fitted curves illustrated by solid lines. (b) Relative position of adsorbed and intercalated Cs, hBN, and the first layer of iridium atoms in the β phase; the sphere sizes indicate the van der Waals radius, ionic radius or nn distance, and relative height extracted from XSW results.

The β phase presents a much larger shift (2.93 eV) of the N 1*s* core level [red curve in Fig. 2(b)]. We link this to the much higher Cs density in the β phase: for the Cs $3d_{5/2}$ intensity ratio between the two phases we find $I_{\mathrm{Cs}}^{\beta}/I_{\mathrm{Cs}}^{\alpha} = 15$. We should point out that the true ratio of Cs density between these two phases is even higher than this value, given that the PE intensity from the intercalated Cs (β_2) is attenuated. In addition to the much stronger shift of the N 1*s* core level, the N 1*s* peak shape is very different from the case of pristine hBN/Ir(111) [20] or the α phase [Fig. 2(b)]: the peak is much broader, and an additional shoulder appears on the low-binding-energy side. One possible explanation is that disordered Cs on top generates an inhomogeneous chemical environment for N.

In order to precisely determine the positions of the different species in the vertical direction, we conducted an XSW measurement on the β phase. In brief, an x-ray standing wave is created by the interference of incident and diffracted x-ray beams. The phase of this standing wave shifts when scanning the beam through the Bragg energy (~2.8 keV), leading to characteristic profiles in the photoemission intensity depending on the position of the emitters in the wave field.

Figure 3(a) presents the XSW analysis of the two components found for Cs $3d_{5/2}$ as well as the full N 1*s* and B 1*s* peaks of the β phase. The circles indicate the measured PE intensity, and the lines are the fitting results [36]. The optimized fitting parameters are summarized in Table II. P^H is the coherent position, and f^H is the coherent fraction. The coherent fraction f^H indicates the width of the distribution of

TABLE II. Fitting parameters for XSW results on the β phase. Errors are $\Delta P^H = \pm 0.01$, $\Delta f^H = \pm 0.04$, $\Delta h = \pm 0.02$ Å.

	P^H	f^H	n	h (Å)
Adsorbed Cs	0.29	0.68	4	9.52
B 1s	0.93	0.68	2	6.50
N 1s	0.88	0.83	2	6.38
Intercalated Cs	0.42	0.93	1	3.15

vertical positions around the average value ($f^H = 1$ for a δ-shaped distribution). The coherent position P^H allows a determination of the height h of the different species, relative to the virtual unrelaxed surface layer of Ir(111). It can be determined using $h = (n + P^H)d_{\mathrm{Ir}(111)}$, where $d_{\mathrm{Ir}(111)} = 2.2167$ Å [33] is the interlayer distance of the Ir crystal in the $\langle 111 \rangle$ direction and n is a suitable integer.

Our choice of the integer n is guided by considering the appropriate diameter of the atoms; see Fig. 3(b) for a sketch drawn to scale. For Ir (gray), the nearest-neighbor (nn) distance ($d_{\mathrm{Ir,nn}} = 2.71$ Å [33]) is used. For N (blue) and B (green) we use the van der Waals diameter ($d_{\mathrm{N,vdW}} = 3.10$ Å, $d_{\mathrm{B,vdW}} = 3.84$ Å [37]). For Cs (pink), we use the ionic diameter ($d_{\mathrm{Cs,ion}} = 3.48$ Å [38]). Within this simplified model we can determine the heights of all atoms (see Table II). Alternative models using the much larger van der Waals radius (6.86 Å [37]) for the intercalated and/or adsorbed Cs or switching the assignment of adsorbed and intercalated Cs do not yield an interpretation consistent with the XSW results.

The relatively high coherent fraction of intercalated Cs is due to the fact that these atoms are directly adsorbed on the flat Ir(111) surface. The coherent fraction of N 1s and B 1s in the β phase is much larger than those in bare hBN/Ir(111) ($f^H_{B\,1s} = 0.28$, $f^H_{N\,1s} = 0.29$) [20]. Thus, Cs intercalation not only lifts hBN up from Ir(111) but also irons out its large-scale corrugation. The intercalated Cs decouples the interaction between hBN and the Ir substrate and relaxes the hBN layer. This finding is in agreement with the previous case with atomic H and CO molecule intercalation [29,30]. However, now a small-scale buckling is present as the average height of all N is lower than that of all B. This average height difference of B and N is surrounding dependent: similar to our β phase, B is positioned slightly farther into the vacuum in hBN/Cu(111) [39], whereas in pristine hBN/Ir(111) it is the other way around [20].

The XSW analysis also yields the PE intensities with hard x rays in the off-Bragg condition of adsorbed β_1 and intercalated β_2. We find an intensity ratio of $I^{\beta_1}/I^{\beta_2} = 1.64$. However, this value can be used only as an estimate of the stoichiometric ratio as the signal from intercalated Cs is attenuated by the hBN and the adsorbed Cs on top.

To summarize our structural characterization, the α phase consists of Cs atoms adsorbed on top of hBN in a low concentration, whereas the β phase is formed by Cs atoms both adsorbed and intercalated in a high concentration. With this in mind, we determine the effect of the electric potential $\phi(h)$ due to the Cs^+ ions in close vicinity to the hBN layer on its valence bands. In Fig. 4(a) we present the ARPES mapping of the α phase. The hBN σ bands, degenerate at the Γ point, split into two branches towards higher binding energy. The bottom of the π band is found at the Γ point, and its top is at the K point, where this band also constitutes the valence band maximum (VBM). The Ir bands are visible in the low-binding-energy range (∼1 eV). The band structure of the α phase resembles the one measured on pristine hBN/Ir(111) (not shown, similar to that in Ref. [40]). This similarity between pristine hBN/Ir(111) and the α phase again confirms a weak influence of the adsorbed Cs on the hBN and Ir(111) electronic structure. More careful comparison reveals a small shift at the top of the σ bands [Fig. 4(b)] at the Γ point. Figure 4(d) extracts the PE intensity at the Γ point as a function of binding energy. We can clearly observe a shift of $\Delta E = 0.35$ eV at the top of the σ bands before (black) and after (red) Cs adsorption. The same ΔE can be measured at the bottom of the π band at the Γ point near 8 eV [Fig. 4(d)] and at the top of the π band at the K point [Fig. 4(c)]. In absolute numbers, the VBM shifts from 2.26 eV for hBN/Ir to 2.61 eV due to Cs adsorption. The occurrence of the same ΔE at different positions in the Brillouin zone suggests a rigid shift of the hBN bands (see also Ref. [27]). In contrast, the iridium band at the Γ point stays at 1 eV before and after Cs adsorption [Fig. 4(c)].

In the β phase, the Ir states at the Γ point also stay at around 1 eV in binding energy. However, the high Cs density in the β phase generates a much stronger electric potential $\phi(h_{\mathrm{hBN}})$ than the α phase and thus a much larger shift of the hBN valence bands [Fig. 4(d)]. The top of the hBN σ band moves to 7.41 eV in binding energy, implying $\Delta E = 3.56$ eV [Fig. 4(b)].

The shift can be approximated using vacuum level alignment: as an estimate of the work function of the β phase we use the value for the bulk alkali, which is an established approximation for the case of alkali metals on metal surfaces [41]. The difference of $\Delta\Phi = 3.62$ eV between $\Phi_{\mathrm{Ir}(111)} = 5.76$ eV (all values for Φ taken from Ref. [42]) and $\Phi_{\mathrm{Cs}} = 2.14$ eV is indeed similar to the ΔE we observe. Also for the case of potassium-intercalated hBN, for which Ref. [27] reports $\Delta E = 2.77$ eV, this model can be applied when the system is approximated as hBN/K/Au(111) with $\Delta\Phi = \Phi_{\mathrm{Au}(111)} - \Phi_{\mathrm{K}} = 5.31\ \mathrm{eV} - 2.30\ \mathrm{eV} = 3.01$ eV. However, this simple model can be applied only when the change in the electric potential energy of the hBN is completely due to the change in work function of the substrate. As a counterexample, our α-phase sample, where Cs is adsorbed on top of hBN, clearly does not fulfill the explanation ($\Delta E = 0.35$ eV measured against $\Delta\Phi = 3.62$ eV). This is also the case for Li/hBN/Au, for which experiment ($\Delta E = 0.9$ eV [27]) and the simple model ($\Delta\Phi = 2.41$ eV) disagree.

For a full description of hBN band shift in the β phase, the adsorbed Cs also has to be taken into account. As the electrons from these Cs atoms also transfer to the metal substrate, the adsorbed Cs ions strengthen the electric field $\vec{E}_{\mathrm{el}}(h)$ pointing from the hBN to the metal surface and thus, as a consequence, contribute to the local potential at the hBN layer $\phi(h_{\mathrm{hBN}}) = -\int_{-\infty}^{h_{\mathrm{hBN}}} E_{\mathrm{el}}(h)dh$. The relative contribution of the intercalated and adsorbed Cs to the band shift in the β phase cannot be disentangled in this study since the stoichiometric ratio and detailed charge distribution cannot be determined by our measurements.

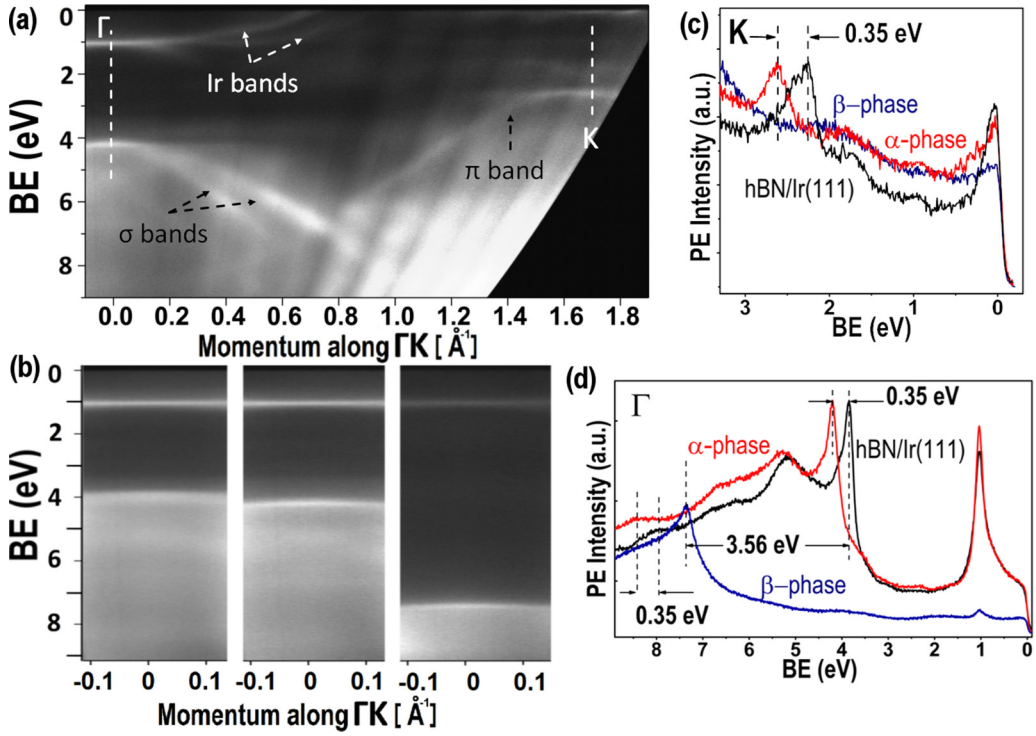

FIG. 4. (a) ARPES results on the α phase. (b) PE intensity mapping around the Γ point, with the horizontal axis as the momentum along the ΓK direction, measured on (left to right) bare hBN/Ir(111), the α phase, and the β phase. (c) PE intensity at the K point versus binding energy measured on bare hBN/Ir(111) (black), the α phase (red), and the β phase (blue). (d) PE intensity at the Γ point versus binding energy measured on bare hBN/Ir(111) (black), the α phase (red), and the β phase (blue).

Under the assumption of a rigid shift, the top of the π band at K (VBM) moves to 5.85 eV. This statement is corroborated by the absence of this band edge down to ~5.0 eV, the maximum binding energy detectable at K with the photon energy used here. No sign of the hBN conduction bands ($\pi^\star$ or $\sigma^\star$) is observed below the Fermi energy [the part around the Γ point is presented in Fig. 4(b), and the one around the K point is given in Fig. 4(c)]. As a consequence, we can give a robust lower bond for the hBN band gap of 5.85 eV. In order to finally detect the conduction band, an even larger band shift is needed, which might be enabled by the use of alkaline-earth metals.

Comparing the core level shift and valence band shift in both the α phase and β phase, we realize that the N and B core levels endure smaller shifts than the valence bands. This agrees with what Fedorov *et al.* observed on the K-decorated hBN [27]. One possible explanation of this smaller shift of core levels is that the N 1s and B 1s orbits reside much deeper in the atomic structure and thus are screened by the electrons in the outer orbitals. The band shifts that can be induced on the wide-band-gap hBN are much larger than the band shifts generated in graphene by charge transfer [43], indicating that the underlying mechanism is different.

IV. CONCLUSION

In conclusion, we have conducted an integrated study on the morphological and electronic structure of Cs functionalized hBN/Ir(111). In this paper, we reported two particular structures: the α phase, where Cs is adsorbed with low density on top of hBN, forming a honeycomb lattice, and the dense β phase, where Cs is both intercalated [in a $(\sqrt{3}\times\sqrt{3})$R30° structure] below and adsorbed on top of hBN (in a disordered way).

In the α phase, the dilute adsorbed Cs hardly changes the morphology of hBN/Ir(111); the influence is mainly on the electronic structure of hBN. We observe a small rigid shift of hBN valence bands [0.35 eV; Figs. 4(c) and 4(d)] and an even smaller (0.04 eV) shift of the N 1s core level to binding energy.

In the β phase, significant geometric changes due to Cs incorporation are observed. Cs intercalation lifts and decouples hBN from the substrate, and the corrugation caused by the moiré modulation is reduced. Cs with high intensity also brings about a large shift of the hBN electronic structure. Compared to the α phase, the shifts in core level (~2.93 eV for N 1s) and in valence bands (~3.56 eV for the top of the σ band) are much larger. Unfortunately, the conduction bands of hBN are still above the Fermi level and thus are undetectable by ARPES. However, based on these facts, we can conclude a lower bond of 5.85 eV for the hBN electronic band gap assuming a rigid shift.

ACKNOWLEDGMENTS

We acknowledge support from the Bonn-Cologne Graduate School of Physics and Astronomy (BCGS, J.C. and W.J.), from CAPES Foundation, Ministry of Education of Brazil (C.C.S), from DAAD/MZOS; from DFG through project BU2197/4-1 (part of SPP 1459 “Graphene”), and from

the University of Cologne via the Advanced Postdoc Grant "2D materials beyond graphene" in the framework of the Excellence Initiative. We appreciate experimental support from the staff at I09.

[1] S. Roth, F. Matsui, T. Greber, and J. Osterwalder, Nano Lett. **13**, 2668 (2013).
[2] J. Hall, B. Pielić, C. Murray, W. Jolie, T. Wekking, C. Busse, M. Kralj, and T. Michely, 2D Mater. **5**, 025005 (2018).
[3] A. Kumar, K. Banerjee, and P. Liljeroth, Nanotechnology **28**, 082001 (2017).
[4] G.-H. Lee, Y.-J. Yu, X. Cui, N. Petrone, C.-H. Lee, M. S. Choi, D.-Y. Lee, C. Lee, W. J. Yoo, K. Watanabe, T. Taniguchi, C. Nuckolls, K. Philip, and J. Hone, ACS Nano **7**, 7931 (2013).
[5] F. Withers, O. Del Pozo-Zamudio, A. Mishchenko, A. Rooney, A. Gholinia, K. Watanabe, T. Taniguchi, S. Haigh, A. Geim, A. Tartakovskii, and K. Novoselov, Nat. Mater. **14**, 301 (2015).
[6] H. Şahin, S. Cahangirov, M. Topsakal, E. Bekaroglu, E. Akturk, R. T. Senger, and S. Ciraci, Phys. Rev. B **80**, 155453 (2009).
[7] J. Zhou, Q. Wang, Q. Sun, and P. Jena, Phys. Rev. B **81**, 085442 (2010).
[8] C. E. Ekuma, V. Dobrosavljević, and D. Gunlycke, Phys. Rev. Lett. **118**, 106404 (2017).
[9] M. Topsakal, E. Aktürk, and S. Ciraci, Phys. Rev. B **79**, 115442 (2009).
[10] X. Blase, A. Rubio, S. G. Louie, and M. L. Cohen, Phys. Rev. B **51**, 6868 (1995).
[11] J. Wu, B. Wang, Y. Wei, R. Yang, and M. Dresselhaus, Mater. Res. Lett. **1**, 200 (2013).
[12] A. Bhattacharya, S. Bhattacharya, and G. P. Das, Phys. Rev. B **85**, 035415 (2012).
[13] M. Liu, Y. Li, P. Chen, J. Sun, D. Ma, Q. Li, T. Gao, Y. Gao, Z. Cheng, X. Qiu, Y. Fang, Y. Zhang, and Z. Liu, Nano Lett. **14**, 6342 (2014).
[14] K. K. Kim, A. Hsu, X. Jia, S. M. Kim, Y. Shi, M. Hofmann, D. Nezich, J. F. Rodriguez-Nieva, M. Dresselhaus, T. Palacios, and J. Kong, Nano Lett. **12**, 161 (2011).
[15] Y. Gao, W. Ren, T. Ma, Z. Liu, Y. Zhang, W.-B. Liu, L.-P. Ma, X. Ma, and H.-M. Cheng, ACS Nano **7**, 5199 (2013).
[16] J. Han, J.-Y. Lee, H. Kwon, and J.-S. Yeo, Nanotechnology **25**, 145604 (2014).
[17] B. Arnaud, S. Lebègue, P. Rabiller, and M. Alouani, Phys. Rev. Lett. **96**, 026402 (2006).
[18] K. Watanabe, T. Taniguchi, and H. Kanda, Nat. Mater. **3**, 404 (2004).
[19] G. Cassabois, P. Valvin, and B. Gil, Nat. Photonics **10**, 262 (2016).
[20] F. H. Farwick zum Hagen, D. M. Zimmermann, C. C. Silva, C. Schlueter, N. Atodiresei, W. Jolie, A. J. Martínez-Galera, D. Dombrowski, U. A. Schröder, M. Will, P. Lazić, V. Caciuc, S. Blügel, T.-L. Lee, T. Michely, and C. Busse, ACS Nano **10**, 11012 (2016).
[21] A. Fedorov, N. Verbitskiy, D. Haberer, C. Struzzi, L. Petaccia, D. Usachov, O. Vilkov, D. Vyalikh, J. Fink, M. Knupfer, B. Büchner, and A. Grüneis, Nat. Commun. **5**, 3257 (2014).
[22] W. Auwärter, M. Muntwiler, T. Greber, and J. Osterwalder, Surf. Sci. **511**, 379 (2002).
[23] B. Ludbrook, G. Levy, P. Nigge, M. Zonno, M. Schneider, D. Dvorak, C. Veenstra, S. Zhdanovich, D. Wong, P. Dosanjh, C. Straßer, A. Stohr, S. Forti, C. Ast, U. Starke, and A. Damascelli, Proc. Natl. Acad. Sci. USA **112**, 11795 (2015).
[24] M. Petrović, I. Š. Rakić, S. Runte, C. Busse, J. T. Sadowski, P. Lazić, I. Pletikosić, Z.-H. Pan, M. Milun, P. Pervan, N. Atodiresei, R. Brako, D. Šokčević, T. Valla, T. Michely, and M. Kralj, Nat. Commun. **4**, 2772 (2013).
[25] J. L. McChesney, A. Bostwick, T. Ohta, T. Seyller, K. Horn, J. González, and E. Rotenberg, Phys. Rev. Lett. **104**, 136803 (2010).
[26] D. Haberer, L. Petaccia, A. V. Fedorov, C. S. Praveen, S. Fabris, S. Piccinin, O. Vilkov, D. V. Vyalikh, A. Preobrajenski, N. I. Verbitskiy, H. Shiozawa, J. Fink, M. Knupfer, B. Büchner, and A. Grüneis, Phys. Rev. B **88**, 081401(R) (2013).
[27] A. Fedorov, C. S. Praveen, N. I. Verbitskiy, D. Haberer, D. Usachov, D. V. Vyalikh, A. Nefedov, C. Wöll, L. Petaccia, S. Piccinin, H. Sachdev, M. Knupfer, B. Büchner, S. Fabris, and A. Grüneis, Phys. Rev. B **92**, 125440 (2015).
[28] T. Ules, D. Lüftner, E. M. Reinisch, G. Koller, P. Puschnig, and M. G. Ramsey, Phys. Rev. B **94**, 205405 (2016).
[29] T. Brugger, H. Ma, M. Iannuzzi, S. Berner, A. Winkler, J. Hutter, J. Osterwalder, and T. Greber, Angew. Chem., Int. Ed **49**, 6120 (2010).
[30] M. L. Ng, A. Shavorskiy, C. Rameshan, A. Mikkelsen, E. Lundgren, A. Preobrajenski, and H. Bluhm, Chem. Phys. Chem. **16**, 923 (2015).
[31] D. Usachov, V. K. Adamchuk, D. Haberer, A. Grüneis, H. Sachdev, A. B. Preobrajenski, C. Laubschat, and D. V. Vyalikh, Phys. Rev. B **82**, 075415 (2010).
[32] I. Horcas, R. Fernández, J. Gomez-Rodriguez, J. Colchero, J. Gómez-Herrero, and A. Baro, Rev. Sci. Instrum. **78**, 013705 (2007).
[33] J. W. Arblaster, Platinum Met. Rev. **54**, 93 (2010).
[34] M. Trzhaskovskaya, V. Nefedov, and V. Yarzhemsky, Atomic Data Nucl. Data Tables **77**, 97 (2001).
[35] M. Kralj, I. Pletikosić, M. Petrović, P. Pervan, M. Milun, A. T. N'Diaye, C. Busse, T. Michely, J. Fujii, and I. Vobornik, Phys. Rev. B **84**, 075427 (2011).
[36] I. A. Vartanyants and J. Zegenhagen, Solid State Commun. **113**, 299 (1999).
[37] M. Mantina, A. C. Chamberlin, R. Valero, C. J. Cramer, and D. G. Truhlar, J. Phys. Chem. A **113**, 5806 (2009).
[38] A. F. Wells, *Structural Inorganic Chemistry* (Oxford University Press, Oxford, 2012).
[39] C. Brülke, T. Heepenstrick, N. Humberg, I. Krieger, M. Sokolowski, S. Weiß, F. S. Tautz, and S. Soubatch, J. Phys. Chem. C **121**, 23964 (2017).
[40] D. Usachov, A. Fedorov, O. Vilkov, V. K. Adamchuk, L. V. Yashina, L. Bondarenko, A. A. Saranin, A. Grüneis, and D. V. Vyalikh, Phys. Rev. B **86**, 155151 (2012).
[41] N. Lang, Phys. Rev. B **4**, 4234 (1971).
[42] H. B. Michaelson, J. Appl. Phys. **48**, 4729 (1977).
[43] U. A. Schröder, M. Petrović, T. Gerber, A. J. Martínez-Galera, E. Grånäs, M. A. Arman, C. Herbig, J. Schnadt, M. Kralj, J. Knudsen, and T. Michely, 2D Mater. **4**, 015013 (2016).